Ocean Engineering 87 (2014) 111–120

Contents lists available at ScienceDirect

Ocean Engineering

journal homepage: www.elsevier.com/locate/oceaneng

Roll damping decay of a FPSO with bilge keel

Gustavo O.G. Avalos [a,*], Juan B.V. Wanderley [a], Antonio C. Fernandes [a], Allan C. Oliveira [b]

[a] COPPE/UFRJ, Rio de Janeiro, RJ, Brazil
[b] Petrobras, Rio de Janeiro, RJ, Brazil

ARTICLE INFO

Article history:
Received 6 August 2013
Accepted 17 May 2014
Available online 14 June 2014

Keywords:
Navier–Stokes
Computational fluid dynamics
Roll damping

ABSTRACT

The roll damping decay is investigated for a Floating Production Storage and Offloading (FPSO). For this purpose, a roll decay test of a middle section of FPSO with bilge keel is simulated by means of the numerical solution of the incompressible two-dimensional Navier–Stokes equations. The governing equations are solved using the finite volume method and the upwind Total Variation Diminishing (TVD) scheme of Roe–Sweby. The upwind TVD scheme resolves and captures the physics of the fluid dynamics without spurious oscillations in regions of the flow field with strong pressure gradients. The numerical results are compared with experimental data for validating the numerical scheme implemented. The simulations indicated the strong influence of the bilge radius in the damping coefficient of the FPSO section. Interesting results were obtained regarding the time series of the displacement of the body and vortex shedding around the bilge keel.

© 2014 Elsevier Ltd. All rights reserved.

1. Introduction

The use of ships converted into FPSO (Floating Production Storage and Offloading) has been widely applied in the field of oil exploration by the advantages it offers, among them, the large load capacity and the reduction of cost and modification time of an existing structure. However, a disadvantage from the start of its application was the poor roll stability.

Wave radiation and viscous effects govern the roll damping of a FPSO. However, Downie et al. (1988) found that the viscous effects are stronger for rectangular hulls due to the generation of large vortices emitted from the sharp edges of the hull surface. The mechanism is non-linear and the intensity of the vortices depends on the amplitude of the roll motion.

It is well known that potential theory reproduces all degrees of freedom of the ship, except the behavior in roll motion because it does not take into account viscous effects on the roll damping, where they are predominant. For example, the study of elongated bilge keels to increase the roll stability proposed by Souza and Fernandes et al. (1998), undertaken by Pinheiro (2003), Fernandes and Oliveira (2009), Oliveira and Fernandes (2011), Oliveira (2011), Oliveira and Fernandes (2012) and Oliveira and Fernandes (2013).

The numerical simulation is another way to study the behavior of ship rolling. The Free-Surface Random-Vortex Method (FSRVM), nonlinear formulation by Yeung (2002) confirmed by computations the problems involving bodies with sharp edges or appendages. The viscous effects play a major role to obtain realistic results. Inviscid-fluid computations do not capture flow separation at appendages. In this case, the added inertia is overestimated and the damping coefficient is underestimated for bodies with sharp edges. Computational work by Kinnas (2005) obtained the same conclusions about viscous effects. (Van't Veer and Fathi 2010) confirmed that the flow memory effects affect the roll damping (Braddock et al., 2005) and (Van't Veer and Fathi 2010) found that when a critical bilge keel height is reached the increasing of height reduces the damping efficiency due to a reduction of interaction between vortex and hull.

In previous work, Avalos and Wanderley (2012) implemented a two-dimensional numerical code to study the roll damping decay of a FPSO with bilge keel, but the bilge radius was not considered correctly because the FPSO section was approximated by a rectangle with sharp edges. The slightly compressible Navier–Stokes equations were solved for the flow around a FPSO section using the finite volume method and the upwind and total variation diminishing (TVD) scheme of Roe (1984) and Sweby (1984). The free surface was considered flat so that wave radiation was not considered. The comparison between the numerical results and the experimental data from Oliveira (2011) showed that the numerical damping was greater than the experimental one. However, since wave radiation was not considered in the numerical simulations, the experimental damping should be a little greater than the numerical one.

In the present work, the correct bilge radius was considered in the numerical simulation and more consistent results were obtained. The experimental damping is now just a little bit greater

* Corresponding author. Tel.: +55 2562 7750.
E-mail address: gustavoomar@oceanica.ufrj.br (G.O.G. Avalos).

http://dx.doi.org/10.1016/j.oceaneng.2014.05.008
0029-8018/© 2014 Elsevier Ltd. All rights reserved.

Nomenclature

a	sound velocity
B	breadth of the model
C_x	force coefficient in the x-direction
C_{xp}	pressure force coefficient in the x-direction
C_{xv}	viscous force coefficient in the x-direction
C_y	force coefficient in the y-direction
C_{yp}	pressure force coefficient in the y-direction
C_{yv}	viscous force coefficient in the y-direction
C_I	dimensionless moment of inertia of the model
C_θ	moment coefficient of the model respect to center of gravity
$C_{\theta p}$	pressure moment coefficient of the model respect to center of gravity
$C_{\theta v}$	viscous moment coefficient of the model respect to center of gravity
C_μ	dimensionless mass of the model
E_e	inviscid flux vector in the x-direction
E_v	viscous flux vector in the x-direction
F_e	inviscid flux vector in the y-direction
F_p	pressure force
F_x	force in the x-direction
F_{xp}	pressure force in the x-direction
F_{xv}	viscous force in the x-direction
F_y	Force in the y-direction
F_{yp}	pressure force in the y-direction
F_{yv}	viscous force in the y-direction
F_v	viscous flux vector in the y-direction, or, viscous force
F_r	Froude number
g	acceleration of gravity
I_{CG}	moment of inertia of the model
k	subscript, indicates the element with respect to the row of a vector
L	length of the model
M	Mach number
M_θ	moment respect to center of gravity of the model
$M_{\theta p}$	pressure moment with respect to center of gravity of the model
$M_{\theta v}$	viscous moment with respect to center of gravity of the model
m	mass of the model
n	subscript, indicates the direction normal to the surface
$\vec{n}$	normal vector
p	dynamic pressure of the fluid
p_∞	pressure of freestream
P	vector defined by flux vectors P_e and P_v
P_e	vector defined by inviscid flux vectors
P_v	vector defined by viscous flux vectors
Q	conserved variable vector
R_B	reynolds number with respect to the breadth of the model
KC	Keulegan–Carpenter number
S	area
T	draft of the model
t	time
u	x-velocity component
u_c	x-velocity component of a particle of the body
u_{ref}	Reference velocity
v	y-velocity component
v_c	y-velocity component of a particle of the body
V	volume
$\vec{w}$	local velocity of the surface of the control volume
x_{CG}	x-component of center of gravity
y_{CG}	y-component of center of gravity
y_S	y-component of a point on the wet surface of the model
θ	angle of inclination
θ_0	initial amplitude of the decay test
μ	dynamic viscosity
ρ	density
ψ	flux limiter
ω	natural frequency

than the numerical one, indicating the importance of considering the correct bilge radius in the numerical simulations. The wave radiation may, indeed, be considered negligible as discussed by Oliveira (2011).

2. Mathematical formulation

In the present work, the slightly compressible Navier–Stokes equations are solved numerically using the finite volume method and the upwind TVD scheme of Roe (1984) and Sweby (1984) for the flow around a FPSO section in free decay. Eq. (1) presents the governing equations in two-dimensional Cartesian coordinates and written in the conservative form, as in Wanderley and Levi (2005).

$$Q_t+(E_e-E_v)_x+(F_e-F_v)_y=0 \tag{1}$$

where Q is the vector of conserved variables, $E_e$and F_e are inviscid flux vectors and, E_v and F_v are viscous flux vectors, see Eq. (2).

$$Q=\begin{Bmatrix} p \\ u \\ v \end{Bmatrix} \quad E_e=\begin{Bmatrix} pu \\ u^2+p/\rho \\ uv \end{Bmatrix} \quad E_v=\frac{M}{R_e}\begin{Bmatrix} 0 \\ u_x \\ v_x \end{Bmatrix} \quad F_e=\begin{Bmatrix} pv \\ uv \\ v^2+p/\rho \end{Bmatrix} \quad F_v=\frac{M}{R_B}\begin{Bmatrix} 0 \\ u_y \\ v_y \end{Bmatrix}$$

$$R_B=\frac{U_{ref}B}{\upsilon}$$

$$U_{ref}=\theta_0\omega B \tag{2}$$

In the numerical simulations, the free surface is considered flat and the density ρ is fixed in each region containing air and water. The static pressure p is obtained from the solution of the governing equations and the total pressure is obtained by adding the hydrostatic and the static pressure. The value assigned for the Mach number M of 0.2 ensures the incompressibility of the flow. The Reynolds number used during the numerical simulations was 4.0×10^4, the same of the experimental investigation of Oliveira (2011). The reference velocity used to define the Reynolds number is obtained by the product of the initial amplitude of the decay test, the natural frequency, and the model breadth, see Eq. (2). The integral form of the Navier–Stokes equations is shown in Eq. (3).

$$\frac{d\tilde{Q}}{dt}=-\int_S\left(\vec{P}-Q\vec{w}\right)\cdot\vec{n}\,dS \tag{3}$$

where

$$\vec{P}=(E_e-E_v)\,\vec{i}+(F_e-F_v)\,\vec{j} \tag{4}$$

$$\tilde{Q} = V\overline{Q} \tag{5}$$

The variable $\overline{Q}$ represents the average value of Q in a cell with volume V and is attributed to the center of the cell, $\overline{Q}$ is defined by Eq. (6).

$$\overline{Q} = \frac{1}{V}\int_V Q dV \tag{6}$$

The vector $w^{\rightarrow}$ represents the local velocity of the cell surface to take into account the deformation of the finite volumes. In the numerical simulation, the following initial and boundary conditions were imposed.

Initial conditions

$$u = 0 \quad v = 0 \quad p = 1 \tag{7}$$

Free-stream boundary conditions

Left and right boundaries

$$\frac{\partial p}{\partial x} = 0 \quad \frac{\partial u}{\partial x} = 0 \quad \frac{\partial v}{\partial x} = 0 \tag{8}$$

Upper and lower boundaries

$$\frac{\partial p}{\partial y} = 0 \quad \frac{\partial u}{\partial y} = 0 \quad v = 0 \tag{9}$$

No slip boundary conditions

$$u = u_c \quad v = v_c \quad \frac{\partial p}{\partial n} = 0 \tag{10}$$

3. Numerical formulation

Eq. (11) shows an approximation of the integral form of the governing equations applied to a two-dimensional triangular finite volume, Eq. (3). Using this explicit and conservative scheme, the vector of conserved variables is obtained in the finite volume center; this is known as cell center approach. A brief presentation of the numerical scheme is given below. For more details, refer to Toro (1999), Jameson and Mavriplis (1986), and Tannehill et al. (1997).

$$\tilde{Q}_i^{n+1} = \tilde{Q}_i^{n} - \Delta t \sum_{f=1}^{3} [[(\vec{P}_e - Q\vec{w}) \cdot \vec{S}]_{i,f} - [\vec{P}_v \cdot \vec{S}]_{i,f}] \tag{11}$$

where

$$\vec{P}_e = E_e \vec{i} + F_e \vec{j} \quad \vec{P}_v = E_v \vec{i} + F_v \vec{j} \tag{12}$$

In Eq. (11), the inviscid flux vector is approximated using the upwind TVD scheme of Roe (1984) and Sweby (1984), defined in Eq. (13).

$$\left(\vec{P}_e \cdot \vec{S}\right)_{i,f} = \frac{1}{2}[(E_e)_i + (E_e)_j]S_x + \frac{1}{2}[(F_e)_i + (F_e)_j]S_y - \frac{1}{2}\hat{A}_f(Q_j - Q_i) \tag{13}$$

where S_x and S_y are the components of the area vector normal to face f, and the subscript j represents the neighbor elements of the element i, see Fig. 1. The matrix $\hat{A}_f$ in Eq. (13) is the modified flux Jacobean matrix, defined in Eq.(14).

$$\hat{A}_f = T_f \hat{\Lambda} T_f^{-1} \tag{14}$$

In Eq. (14), the matrix $\hat{\Lambda}$ is a diagonal matrix which elements are shown in Eq. (15). In Eq. (15), ΔS is the distance between the finite volume centers i and j, see Fig. 1. In Eq. (14), the matrix T_f is defined in Eq. (16). The nondimensional time step Δt used in Eq. (11) and Eq. (15) was 2.1×10^{-5}.

$$\hat{\lambda}_k = |\lambda_k| + \psi_k\left(\frac{\Delta t}{\Delta S}|\lambda_k|^2 - |\lambda_k|\right) \tag{15}$$

$$T_f = [\vec{x}_1, \vec{x}_2, \vec{x}_3, \vec{x}_4] \tag{16}$$

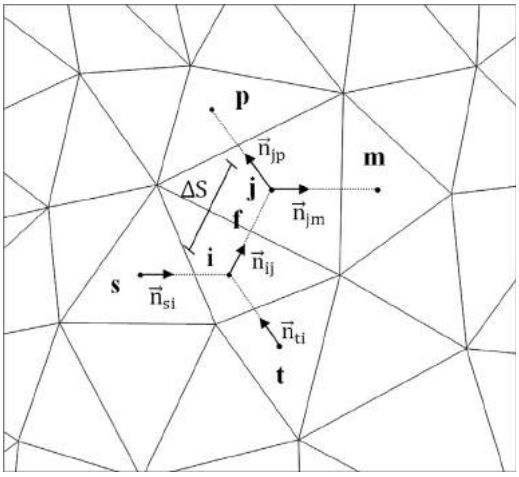


Fig. 1. Location of the elements m, p, s and t respect to the face f between the elements i and j.

In Eqs. (15) and (16), $(x^{\rightarrow}_k, \lambda_k)$ are the eigenvectors and eigenvalues of the Jacobean matrix A, defined in Eq. (17).

$$A = \frac{\partial\left(\vec{P}_e \cdot \vec{S}\right)_{i,f}}{\partial Q_i} \tag{17}$$

In Eq. (15), ψ_k is the Van Leer (1979) flux limiter, defined in Eq. (18). The parameter r_k in Eq. (18) is defined in Eq. (19).

$$\psi_k = \begin{cases} 0 & if \quad r_k \le 0 \\ \dfrac{2r_k}{1+r_k} & if \quad r_k > 0 \end{cases} \tag{18}$$

$$r_k = \frac{\Delta_{upw}}{\Delta_{loc}} = \begin{cases} \dfrac{\vec{B} \cdot \vec{n}_{ij}}{(\Delta w_k)_{ij}} & if \quad \lambda_k \le 0 \\ \dfrac{\vec{D} \cdot \vec{n}_{ij}}{(\Delta w_k)_{ij}} & if \quad \lambda_k > 0 \end{cases} \tag{19}$$

where $\vec{n}_{ij}$ represents an unit vector between the grid elements i and j. $(\Delta w_k)_{ij}$ are the components of the vector $\Delta\vec{w}_{ij}$, given in Eq. (20). The vectors $\vec{B}$ and $\vec{D}$ are defined in Eq. (21), where the subscripts m, p, s, and t are the grid elements shown in the Fig. 1.

$$\Delta\vec{w}_{ij} = T_f(Q_j - Q_i) \tag{20}$$

$$\vec{B} = (\Delta w_k)_{jm}\vec{n}_{jm} + (\Delta w_k)_{jp}\vec{n}_{jp}$$

$$\vec{D} = (\Delta w_k)_{si}\vec{n}_{si} + (\Delta w_k)_{ti}\vec{n}_{ti} \tag{21}$$

In Eq. (11), the viscous flux vector is approximated as shown in Eq. (22).

$$\left(\vec{P}_v \cdot \vec{S}\right)_{i,f} = \frac{1}{2}[(E_v)_i + (E_v)_j]S_x + \frac{1}{2}[(F_v)_i + (F_v)_j]S_y \tag{22}$$

4. Equations of motion

The non-dimensional equations of motion are presented in Eq. (23) and the initial conditions are given in Eq. (24). The coefficients of moment C_θ, horizontal force C_x, and vertical force C_y are obtained by integration of the pressure and viscous stress on the submerged part of the body surface.

$$2C_I\ddot{\theta}_{CG} = C_\theta \quad \text{roll}$$

$$2C_\mu\ddot{x}_{CG} = C_x \quad \text{sway}$$

$$2C_\mu \ddot{y}_{CG} = C_y - 2\left(\frac{M}{Fr}\right)^2 C_\mu \quad \text{heave} \tag{23}$$

where

$$Fr = \frac{U_{ref}}{\sqrt{gB}}$$
$$U_{ref} = \theta_0 \omega B$$
$$\dot{\theta}(t=0) = 0 \quad , \quad \theta(t=0) = \theta_0$$
$$\dot{x}(t=0) = 0 \quad , \quad x(t=0) = x_{CG}$$
$$\dot{y}(t=0) = 0 \quad , \quad y(t=0) = y_{CG} \tag{24}$$

where, M and Fr are Mach and Froude numbers, respectively, where $M=0.2$ for incompressible flows and $Fr=0.21$. The non-dimensional form of inertia moment and mass of the FPSO are shown in Eq. (25). The coefficients C_θ, C_x, and C_y are calculated according to Eqs. (26)–(28), where the subscripts v and p represent viscous and pressure parts, respectively.

$$C_I = \frac{I}{\rho B^4 L} \quad C_\mu = \frac{m}{\rho B^2 L} \tag{25}$$

$$C_\theta = C_{\theta p} + C_{\theta v}$$
$$C_{\theta p} = \frac{M_{\theta p}}{(1/2)\rho a^2 B^2 L} \quad C_{\theta v} = \frac{M_{\theta v}}{(1/2)\rho a^2 B^2 L} \tag{26}$$

$$C_x = C_{xp} + C_{xv}$$
$$C_{xp} = \frac{F_{xp}}{(1/2)\rho a^2 BL} \quad C_{xv} = \frac{F_{xv}}{(1/2)\rho a^2 BL} \tag{27}$$

$$C_y = C_{yp} + C_{yv}$$
$$C_{yp} = \frac{F_{yp}}{(1/2)\rho a^2 BL} \quad C_{yv} = \frac{F_{yv}}{(1/2)\rho a^2 BL} \tag{28}$$

The forces and moment acting on the FPSO, see Fig. 2, are obtained by integration of the pressure and viscous stress around the submerged part of the body, see Eqs. (29) and (30). The hydrostatic pressure is taken into account in the calculation of the pressure force and moment.

$$F_p = -\int_S (p - p_\infty - \rho g y)\vec{n}\, dS$$
$$F_v = -\int_S \left(\bar{\bar{\tau}} \cdot \vec{n}\right) dS \tag{29}$$

$$M_{\theta p} = \int_S (p - p_\infty - \rho g y)\vec{r}\, x\, \vec{n}\, dS$$
$$M_{\theta v} = \int_S \vec{r}\, x \left(\bar{\bar{\tau}} \cdot \vec{n}\right) dS \tag{30}$$

where

$$r = (x - x_{CG})\vec{i} + (y - y_{CG})\vec{j} \tag{31}$$

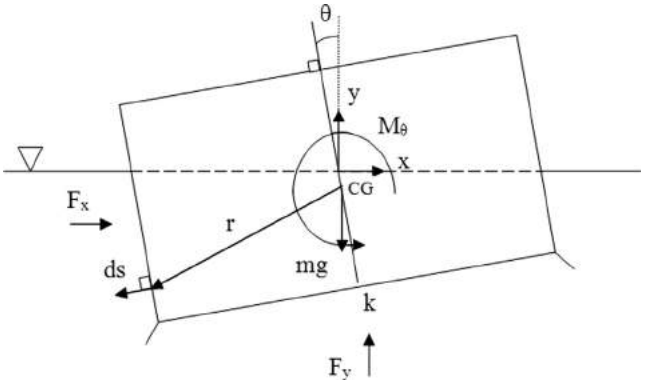


Fig. 2. Forces acting on the cross section of a FPSO.

The equations of motion are solved using the second order Lax–Wendroff and the Euler explicit methods to compute the position and velocity of the body, respectively, see Eqs. (32) and (33).

$$\theta^{n+1} = \theta^n + \dot{\theta}^n \Delta t + 1/2\ddot{\theta}^n \Delta t^2$$
$$x^{n+1} = x^n + \dot{x}^n \Delta t + 1/2\ddot{x}^n \Delta t^2$$
$$y^{n+1} = y^n + \dot{y}^n \Delta t + 1/2\ddot{y}^n \Delta t^2 \tag{32}$$

$$\dot{\theta}^{n+1} = \dot{\theta}^n + \ddot{\theta}^n \Delta t$$
$$\dot{x}^{n+1} = \dot{x}^n + \ddot{x}^n \Delta t$$
$$\dot{y}^{n+1} = \dot{y}^n + \ddot{y}^n \Delta t \tag{33}$$

5. Generation and deformation of the grid

The unstructured grid is generated using the Delaunay method, except around the body. In this case, the front advance method is used in order to improve the boundary layer capturing, see Fig. 3 and Fig. 4.

Fig. 3 shows the concentration of grid elements around the free surface in order to capture more accurately the flow properties in this

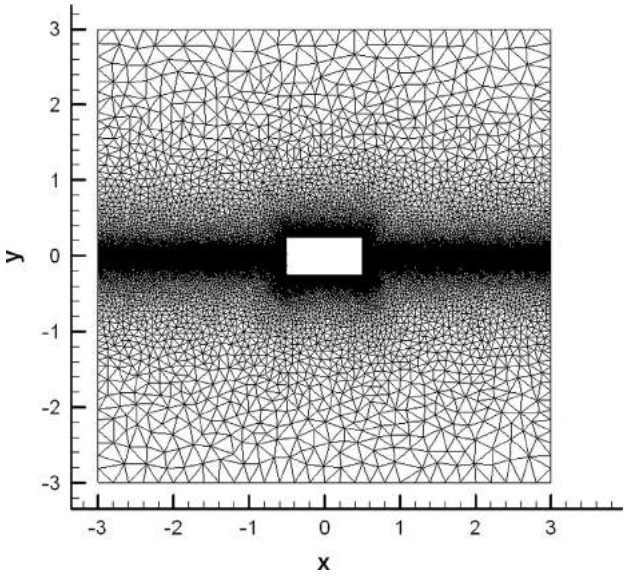


Fig. 3. Computational grid around the FPSO.

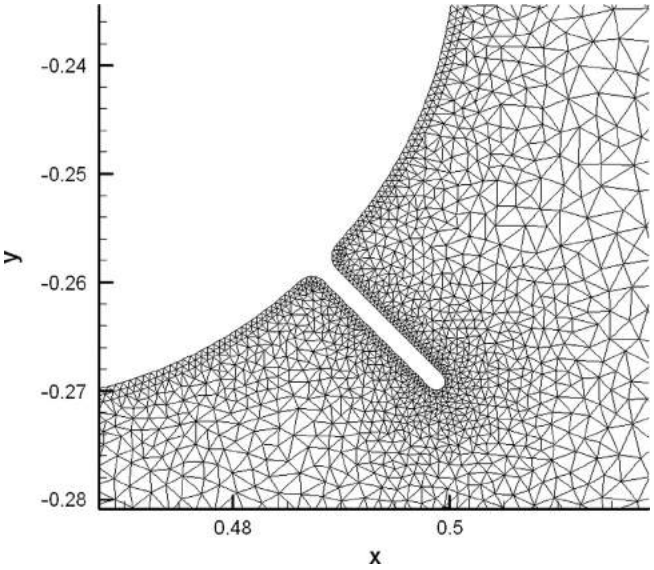


Fig. 4. Computational grid around the surface of FPSO near bilge keel.

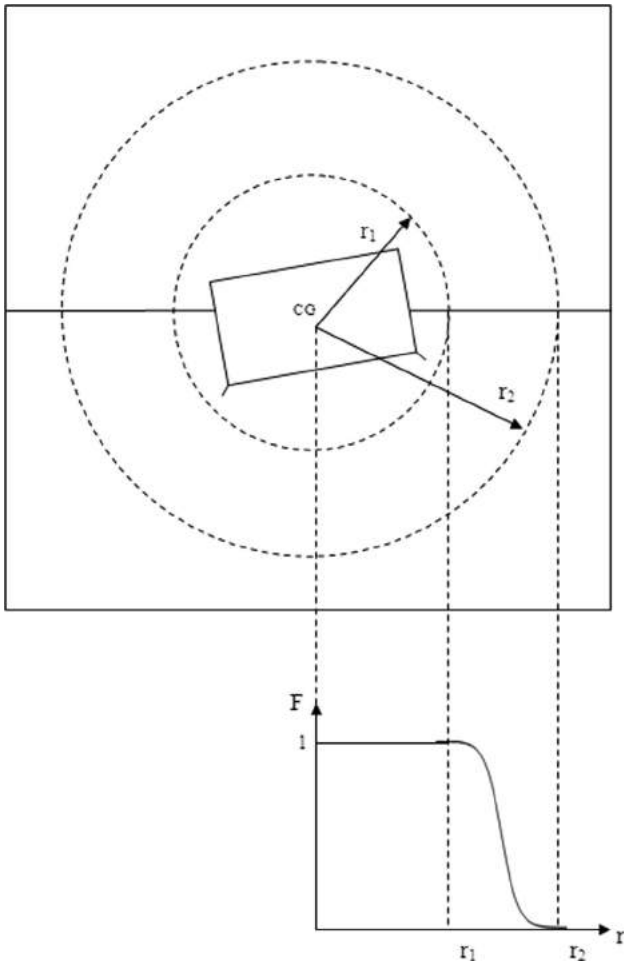


Fig. 5. Function *F*.

region. For the case of bilge keel b075, two different grids were tested, one with 85657 and the other with 151762 elements. The obtained numerical results were the same for both grids. Therefore, the grid with 151762 elements was adopted in the entire numerical simulation. Since this is a transient simulation, a grid with more elements was not used because it would demand more computational time.

The grid is constructed in such a way that the boundary of body is part of the grid. Then, it is necessary to displace the grid points to follow the motion of the body. In this case, the displacement of grid points follows the body motion according to the function *F*. This function varies between zero and one as a function of the position of the grid point with respect to the center of gravity of the body, as given in Eq. (34). The function *F* is represented in the Fig. 5. The product between the displacement of the body center of gravity and function *F* provides the displacement of the grid point.

$$F = \begin{cases} 1 & r < r_1 \\ \frac{1+\tanh(\arg)}{2} & r_1 \le r \le r_2 \\ 0 & r_2 > r \end{cases} \tag{34}$$

where

$$\arg = 4\left(1 - \frac{2(r-r_1)}{r_2-r_1}\right) \tag{35}$$

6. FPSO model Properties

Oliveira (2011) conducted several roll decay tests using a FPSO model section. See also (Oliveira and Fernandes, 2012). The model characteristics and bilge keel heights are shown in Tables 1 and 2, respectively. The angle of initial displacement of the body to be analyzed here is 12°. A sketch of the FPSO section is shown in Fig. 6.

The codes used to designate each bilge keel represent the height of each bilge keel in the prototype. For example, bilge keel b180 has a height of 1.80 m in the prototype which corresponds to a height of 0.024 m in the 1/75 scale model.

7. Results

Fig. 7(a)–(d) show the numerical results obtained in the present study and the experimental results obtained by Oliveira (2011) (also in (Oliveira and Fernandes, 2012) with and without bilge keel. The agreement between numerical and experimental results for the decay test is much better for the case with bilge keel than without. In the case without bilge keel, it is likely that the wave radiation (not considered here) cannot be neglected. Also, as shown by Oliveira and Fernandes (2013) the vortices are attracted to the bottom (what is not happening with the case with bilge keels) leading to more complex flows.

There is a good agreement between numerical and experimental results for the case with bilge keel. The numerical results are a little less damped than the experimental data probably because wave radiation is not considered in the numerical simulation.

Table 1
Model characteristics of FPSO.

Characteristics of model	Magnitude
Breadth (*B*)	0.725 m
Draft (*T*)	0.196 m
Lentgh(*L*)	0.90 m
Center of gravity (KG)	0.175 m
Radius de gyration (R_{xx})	0.264 m
Mass per unit length (m/L)	169.76 Kg/m
Transverse moment of inertia per unit length(I_{CG}/L)	13.269 Kg/m
Oscillation period for rolling	1.74 s
Bilge radius	0.030 m

Table 2
Bilge keels of testing decay of Oliveira.

Bilge keel	Magnitude (m)
b075	0.010
b120	0.016
b180	0.024



Fig. 6. Model of FPSO section in the Laboratory of Wave and Flow, LOC-COPPE/UFRJ.

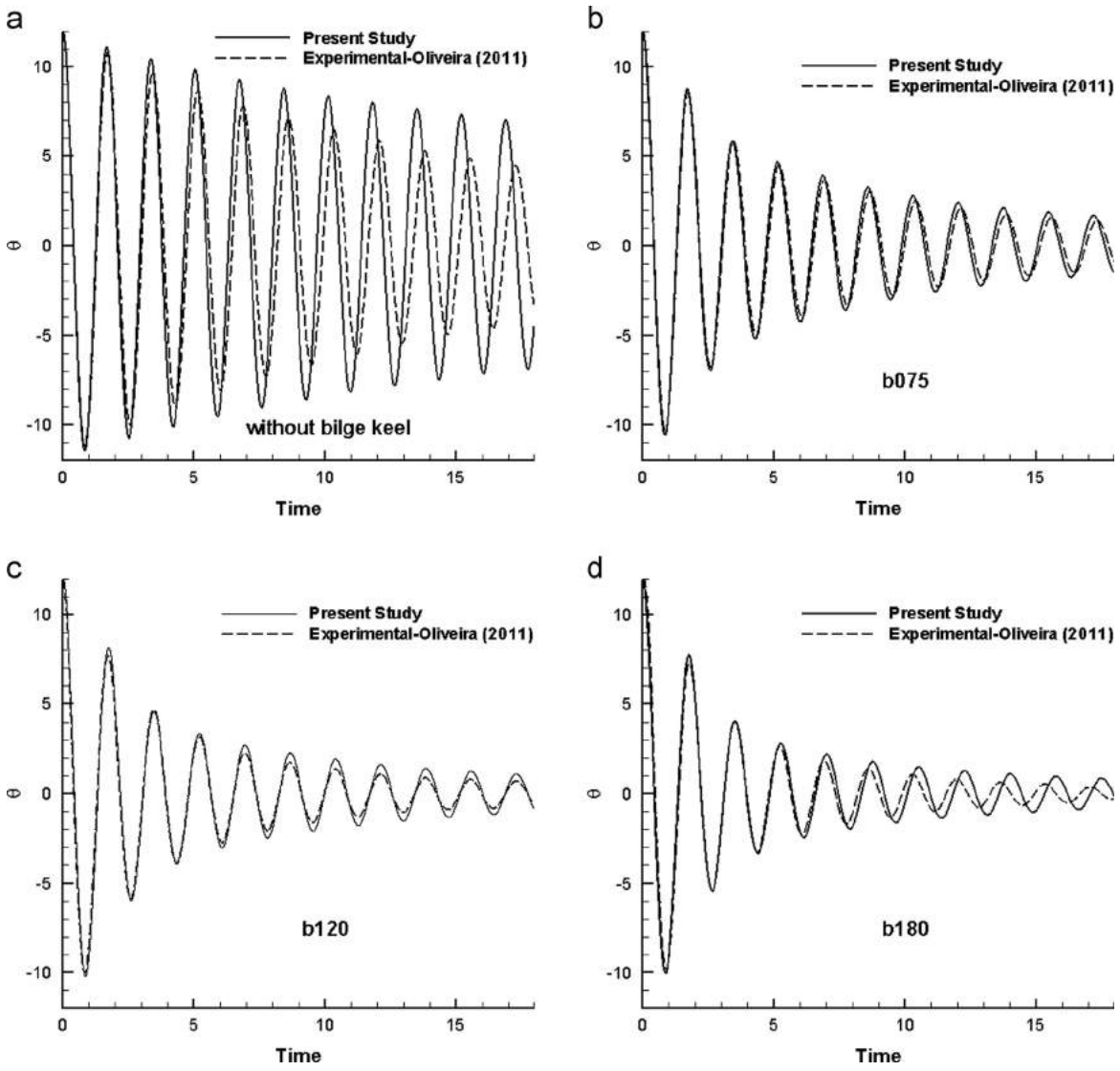


Fig. 7. Numerical and Experimental Roll Decay Test-I.

The agreement for the oscillation period is not so good in the last oscillations for the case with larger bilge keel; see Fig. 7(d). Despite of these differences it can be confirmed that the vortex shedding viscous effects govern the roll damping decay in this case.

The dynamics of the vortices generated around each bilge keel (case b120) is shown in Fig. 8. The vortices generated in each bilge keel are always generated throughout each half oscillation.

In the second oscillation, the third vortex generated in each bilge keel interacts destructively with the previous one, see Fig. 8(c)–(e). From the third oscillation, vortices behave orderly. These vortices are shed sequentially at an angle of 45° with respect to the mean position of the bilge keel, also observed in Oliveira (2011). This behavior is probably happening because the front vortex being more intense is dragging the rear vortex that is less intense.

The vortex dynamics for the cases of bilge keels b075 and b180 is similar to the case of bilge keel b120. There is a difference in the size of the initial vortices which depend on the height of each bilge keel. For the case of bilge keel b075, no vortex shedding is observed at an angle of 45°, in this case, the vortices are shed to the bottom and side wall of the FPSO, but near to the bilge keels.

In the case without bilge keel, the dynamics of the vortices and the mechanism of vortex generation around the bilge are different. The initial vortices are small and vortices are always shed to the bottom and side wall of the FPSO, see Fig. 9(b) and (d). The vortices are not generated throughout each half oscillation, but when the next half oscillation begins, see Fig. 9(a) and (b).

An additional interesting result is shown in Fig. 10(a), numerical results with sharp and rounded bilges. The result with sharp bilges is more damped than the one for rounded bilges. Fig. 10(b) shows the experimental result from Oliveira (2011) for the bilge keel b075 and the numerical result for the bilge keel b075, but considering sharp bilges instead of rounded bilges. In this case, it can be observed that the numerical result is more damped than experimental one. The distance between the center of gravity of the FPSO section and the center of pressure of the bilge keel mounted on the sharp bilge is greater than the one of the bilge keel mounted on the rounded bilge, which may explain why, in this case, the numerical result is more damped that the experimental data.

The damping ratio for the roll damping decay of a FPSO section with bilge keel is presented in Fig. 11. The damping ratio is obtained using Eq. (36), from Oliveira (2011).

$$Zeta = \frac{\delta}{\sqrt{(2\pi)^2 + \delta^2}} \tag{36}$$

where δ is the logarithmic decrement of the amplitude.

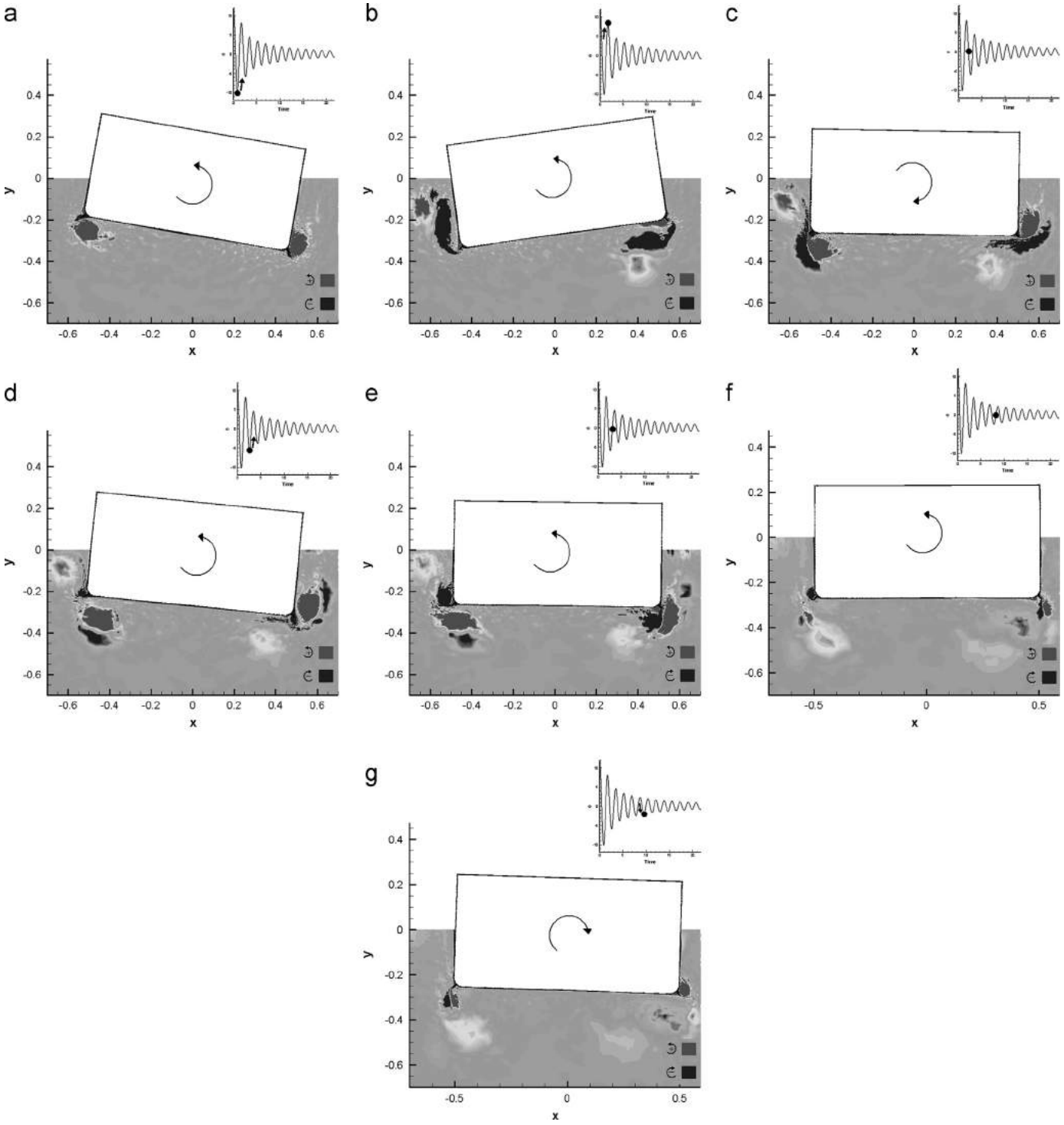


Fig. 8. Vortices field around the FPSO with bilge keel b120.

It can be seen that the numerical results reproduce the qualitative behavior of the experimental damping coefficient at large amplitudes of oscillation. It is observed the damping coefficient saturation as observed in Oliveira (2011) and Oliveira and Fernandes (2012), see Fig. 11(a)–(d). The numerical result behaves more orderly than the experimental data. At small amplitudes, the numerical damping coefficient converges to a well defined region, see Fig. 11(d). This cannot be confirmed experimentally because, as explained in Oliveira (2011) and Oliveira and Fernandes (2012), the uncertainly analysis of the experimental set up shows that the error increase hyperbolically as the small angles decrease to zero, see Fig. 11(e). Based on the current experimental set ups, the CFD analysis maybe the only way to access the small angle region correctly.

8. Conclusion

The numerical code developed in this work, based on the finite volume method using the upwind and total variation diminishing (TVD) scheme of Roe (1984) and Sweby (1984), proved to be a useful tool to study the roll damping decay of FPSO. The numerical

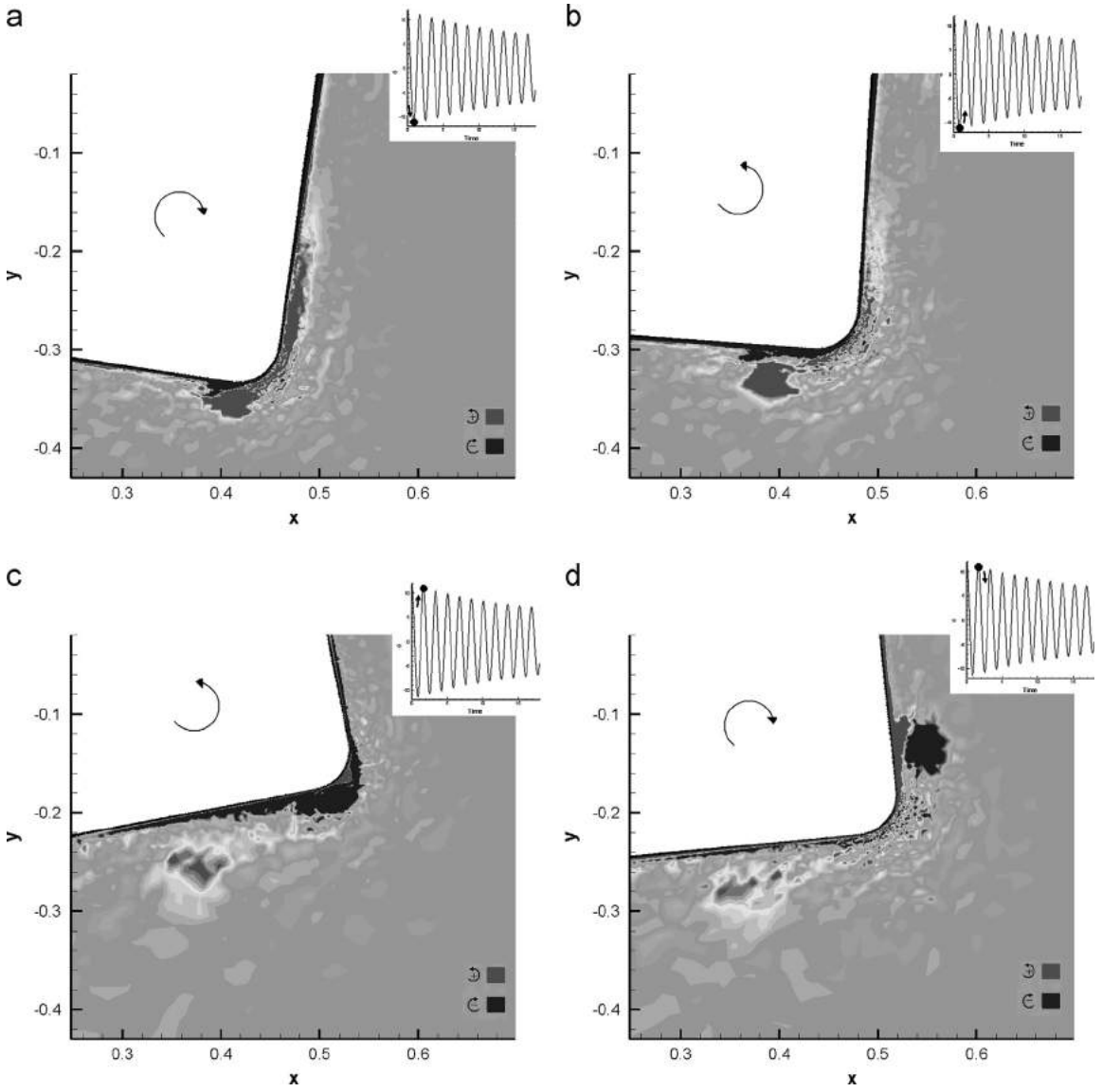


Fig. 9. Vortices field around the FPSO without bilge keel.

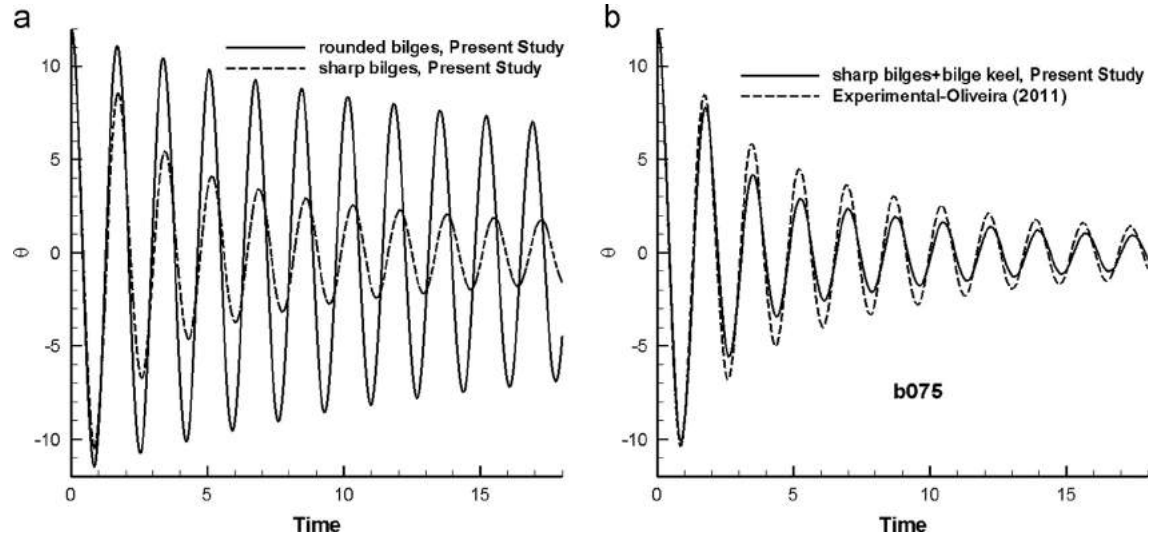


Fig. 10. Numerical and Experimental Roll Decay Test-II.

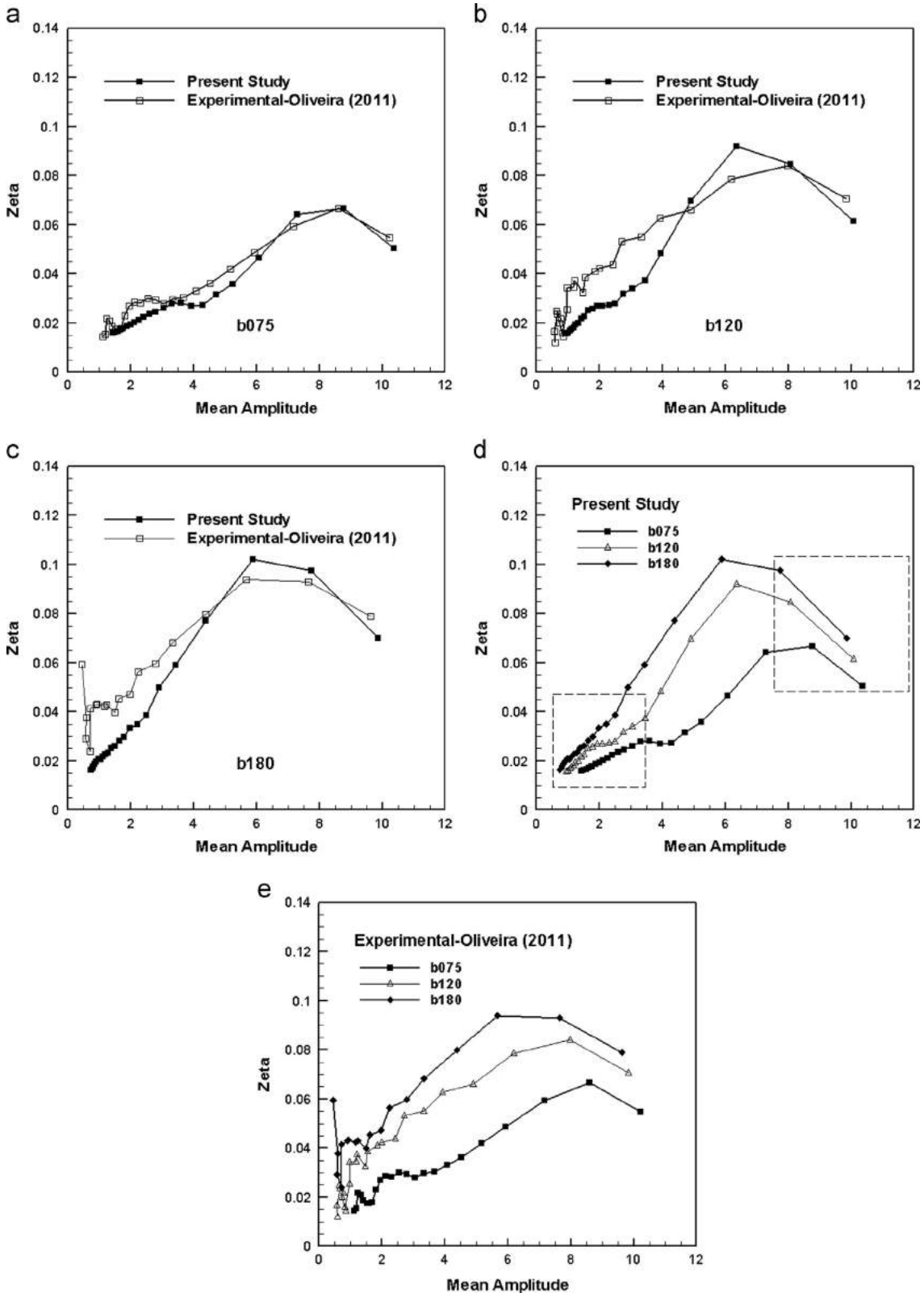


Fig. 11. Numerical and Experimental Roll decay decrement.

results obtained for the FPSO with bilge keel agree well with the experimental data.

The numerical simulation confirms the vortices that are shed sequentially at an angle of 45° with respect to the mean position of the bilge keel, also observed in Oliveira (2011). This behavior is probably happening because the front vortex being more intense is dragging the rear vortex that is less intense.

The size of the vortices shed from each bilge keel depends on the bilge keel height and the amplitude to which starts every half oscillation, more precisely, it depends on the *KC* number.

The vortices generated in each bilge keel are always generated throughout each half oscillation. In the case with rounded bilges, the vortices are generated when the next half oscillation begins.

The numerical results with sharp bilges are more highly damped than with rounded bilges, therefore the roll damping is greatly influenced by the bilge radius, too.

The numerical results confirm the increase of damping coefficient with the height of the bilge keel. It is also important to note that, as observed in Oliveira (2011) and Oliveira and Fernandes (2012), the present work confirmed the occurrence of the so-called damping coefficient saturation. That is, the damping coefficient does not increase with amplitude as predicted by conventional quadratic theory; see Oliveira and Fernandes (2012).

It was observed a smoother variation of the numerical damping coefficient than the experimental one. For lower amplitudes, the damping coefficient converges to a well defined region.

The comparison between the numerical and experimental results demonstrates that approximating the free surface as a flat surface is acceptable. The damping of FPSO due to wave radiation is negligible in the case with bilge keel.

Future works will investigate the influence of wave radiation on the damping coefficient.

References

Avalos, G.O.G., Wanderley, J.B.V., A Two dimensional Numerical Simulation of Roll Damping Decay of a FPSO using the upwind TVD scheme of Roe–Sweby. In: Proceedings of the 31st OMAE, Rio de Janeiro.

Braddock, R.A., Timms, R.J., Thiagarajan, K.P., June 12–17, 2005. A Comparison of Experiment and FRSV modeling of larger than normal bilge keels, In: Proceedings of the 24th Offshore Mechanics and Arctic Engineering (OMAE), Halkidiki, Greece.

Downie, M.J., Bearman, P.W., Graham, J.M.R., 1988. The effect of vortex shedding on the coupled roll response of bodies in waves. J. Fluid Mech. 189, 243–264.

Fernandes, A.C., Oliveira, A.C., June, 2009. The Roll Damping Assessment via Decay Model Testing (New Ideas about an Old Subject). Journal of Marine Science and Application,Springer-Verlag and Harbin Engineering University, ISSN: 1671-9433 (Print) 1993-5048 (Online), DOI: 10.1007/s11804-009-8107-z,Volume 8, Number 2, pp. 144–150.

Jameson, A., Mavriplis, D., 1986. Finite Volume Solution of the Two-Dimensional Euler Equations on Regular Triangular Mesh. AIAA J. 24 (4), 611–618.

Kinnas, S.A., 2005. FPSO Roll Motions. Final Project Report, Austin, Texas.

Oliveira, A.C., Fernandes, A.C., 2011. Roll Damping of Flat-Bottom Hulls: Critique of the Quadratic Reason Marine Technology and Engineering. In: Guedes Soares, C., et al. (Eds.), Marine Environment, Dynamics and Hydrodynamics, Vol. 1. Publisher: Taylor and Francis Group, London, UK.

Oliveira, A.C., 2011. Novas abordagens para análise do amortecimento não linear do balanço transversal de FPSOs, Tese de D.Sc, COPPE/UFRJ, Rio de Janeiro, RJ, Brasil, (in Portuguese).

Oliveira, A.C., Fernandes, A.C., 2013. The Non-Linear Roll Damping of a FPSO Hull, Trans. ASME (American Society of Mechanical Engineers). J. Offshore Mech. Arct. Eng..

Oliveira, A.C. and Fernandes, A.C., July 1–5, 2012. An Empirical Nonlinear Model to Estimate FPSO with Extended Bilge Keel Roll Linear Equivalent Damping in Extreme Seas. In: XXXI International Conference on Ocean, Offshore and Arctic Engineering (OMAE). paper OMAE2012-83360, Rio de Janeiro, Brazil.

Pinheiro, K.A.G., 2003. Controle de Balanço Transversal de FPSOs. Trabalho de Formatura, UFRJ, Rio de Janeiro.

Roe, P.L., 1984. Generalized formulation of TVD Lax–Wendroff scheme. ICASE Report 84–53.

Souza, J.R., Fernandes, A.C., Masetti, I.Q., da Silva, S. and Kroft,S.A.B., 1998. Nonlinear Rolling of an FPSO with larger-than-usual Bilge Keels. In: Proceedings of the 17th OMAE, Lisbon.

Sweby, P.K., 1984. High resolution scheme using flux limiter for hiperbolic conservation laws. SIAM J. Fluid Numer. Anal. 21, 995–1011.

Tannehill, J.C., Anderson, D.A., Pletcher, R.H., 1997. Computational Fluid Mechanics and Heat Transfer, Second Edition McGraw-Hill, New York.

Toro, E.F., 1999. Riemann Solvers and Numerical Methods for Fluid Dynamics: A Practical Introduction, Second edition Springer–Verlag, New York.

Van Leer, B., 1979. Towards the ultimate conservative difference scheme, V: a second-order sequel to Godunov's method. J. Comput. Phys. 32, 101–136.

Yeung, R.W., May 26–31, 2002. Fluid dynamics of finned bodies–from VIV to FPSO, In: Proceedings of 12th International Offshore and Polar Engineering Conference (ISOPE), Kitakyushu, Japan.

Van't Veer, R., Fathi, F., 2010. On roll hydrodynamics of FPSO's fitted with riser balcony and bilge keels. In: RINA William Froude Conference: Advances in Theorical and Applied Hydrodynamics, Portsmouth, UK.

Wanderley, J.B.V., Levi, C.A., 2005. Vortex induced loads on marine risers. Ocean Eng. 32, 1281–1295.